The Meteoritical Society

Meteoritics & Planetary Science 49, Nr 9, 1594–1611 (2014)
doi: 10.1111/maps.12206

Stardust Interstellar Preliminary Examination V: XRF analyses of interstellar dust candidates at ESRF ID13

Frank E. BRENKER[1], Andrew J. WESTPHAL[2*], Laszlo VINCZE[3], Manfred BURGHAMMER[4], Sylvia SCHMITZ[1], Tom SCHOONJANS[3], Geert SILVERSMIT[3], Bart VEKEMANS[3], Carlton ALLEN[5], David ANDERSON[2], Asna ANSARI[6], Saša BAJT[7], Ron K. BASTIEN[8], Nabil BASSIM[9], Hans A. BECHTEL[10], Janet BORG[11], John BRIDGES[12], Donald E. BROWNLEE[13], Mark BURCHELL[14], Anna L. BUTTERWORTH[2], Hitesh CHANGELA[15], Peter CLOETENS[4], Andrew M. DAVIS[16], Ryan DOLL[17], Christine FLOSS[17], George FLYNN[18], Patrick FOUGERAY[19], David R. FRANK[8], Zack GAINSFORTH[2], Eberhard GRÜN[20], Philipp R. HECK[21], Jon K. HILLIER[21], Peter HOPPE[22], Bruce HUDSON[23], Joachim HUTH[22], Brit HVIDE[6], Anton KEARSLEY[24], Ashley J. KING[6], Barry LAI[25], Jan LEITNER[22], Laurence LEMELLE[26], Hugues LEROUX[27], Ariel LEONARD[17], Robert LETTIERI[2], William MARCHANT[2], Larry R. NITTLER[28], Ryan OGLIORE[29], Wei Ja ONG[17], Frank POSTBERG[21], Mark C. PRICE[14], Scott A. SANDFORD[30], Juan-Angel Sans TRESSERAS[4], Alexandre S. SIMIONOVICI[31], Vicente A. SOLÉ[4], Ralf SRAMA[32], Frank STADERMANN[17], Thomas STEPHAN[16], Veerle J. STERKEN[32], Julien STODOLNA[2], Rhonda M. STROUD[9], Steven SUTTON[25], Mario TRIELOFF[33], Peter TSOU[34], Akira TSUCHIYAMA[35], Tolek TYLISZCZAK[10], Joshua Von KORFF[2], Naomi WORDSWORTH[36], Daniel ZEVIN[2], Michael E. ZOLENSKY[5], and >30,000 STARDUST@HOME[37]

[1]Goethe University Frankfurt, Altenhoeferallee 1, 60438, Frankfurt am Main, Germany
[2]Space Sciences Laboratory, University of California at Berkeley, Berkeley, California 94720, USA
[3]Department of Analytical Chemistry, Ghent University, Krijgslaan 281 S12, B-9000 Ghent, Belgium
[4]European Synchrotron Radiation Facility (ESRF), 6 rue Jules Horowitz, F-38043 Grenoble, France
[5]Astromaterials Acquisition
[6]Robert A. Pritzker Center for Meteoritics and Polar Studies, The Field Museum of Natural History, Chicago, Illinois 60605–2496, USA
[7]DESY, Notkestr. 85, Geb. 99, 22607 Hamburg, Germany
[8]ESCG, NASA/Johnson Space Center, Mail Code KT, 2101 NASA Parkway, Houston, Texas 77058, USA
[9]Nanoscale Materials Section, Naval Research Laboratory, 4555 Overlook Ave SW, Washington, District of Columbia 20375, USA
[10]Advanced Light Source, Lawrence Berkeley Laboratory, 1 Cyclotron Road, MS 6-2100, Berkeley, California 94720, USA
[11]IAS Orsay, Orsay, France
[12]Department of Physics and Astronomy, Space Research Centre, University of Leicester, LE1 7RH Leicester, UK
[13]Department of Astronomy, University of Washington, Seattle, Washington 98195, USA
[14]University of Kent, Canterbury, Kent CT2 7NR, UK
[15]George Washington University, 2121 I St NW, Washington, District of Columbia 20052, USA
[16]University of Chicago, 5734 South Ellis Avenue, Chicago, Illinois 60637, USA
[17]Washington University in St. Louis, Campus Box 1105, One Brookings Drive, St. Louis, Missouri 63130, USA
[18]Department of Physics, SUNY–Plattsburgh, Ward 218, 101 Broad St., Plattsburgh, New York 12901, USA
[19]Chigy, Burgundy, France
[20]Max-Planck-Institut für Kernphysik, Saupfercheckweg 1, Heidelberg D-69117, Germany
[21]Institut für Geowissenschaften, Im Neuenheimer Feld 234-236, 69120 Heidelberg, Germany
[22]Max Planck Institute for Chemistry, Hahn-Meitner-Weg 1, 55128 Mainz, Germany
[23]615 William St., Apt 405, Midland, Ontario, Canada
[24]Natural History Museum, Cromwell Road, London SW7 5BD, UK
[25]Advanced Photon Source, Argonne National Laboratory, 9700 South Cass Ave., Argonne, Illinois 60439, USA
[26]Ecole Normale Superieure de Lyon, Lyon, France

© The Meteoritical Society, 2014.

[27]Unite Materiaux et Transformations—UMR 8207, Universite Lille 1, 59655 Villeneuve d'Ascq, France
[28]Department of Terrestrial Magnetism, Carnegie Institution of Washington, 5241 Broad Branch Road NW, Washington, District of Columbia 20015, USA
[29]Hawaii Institute of Geophysics and Planetary Sciences, School of Ocean and Earth Sciences and Technology, University of Hawaii at Manoa, 1680 East-West Road, Post 602, Honolulu, Hawai'i 96822, USA
[30]Astrophysics Branch, NASA-Ames Research Center, Mail Stop 245-6, Bldg N245, Room 112, Moffett Field, California 94035, USA
[31]Institut des Sciences de la Terre, Observatoire des Sciences de l'Univers de Grenoble, Grenoble, France
[32]Institut für Raumfahrtsysteme, Universität Stuttgart, Raumfahrtzentrum Baden Württemberg, Pfaffenwaldring 29, 70569 Stuttgart, Germany
[33]Institut für Geowissenschaften, Im Neuenheimer Feld 234-236, 69120 Heidelberg, Germany
[34]Jet Propulsion Laboratory, 4800 Oak Grove Blvd, Pasadena, California 91109, USA
[35]Department of Earth and Planetary Science, Graduate School of Science, Osaka University, Osaka, Japan
[36]South Buckinghamshire, UK
[37]Worldwide
*Corresponding author. E-mail: westphal@ssl.berkeley.edu

(Received 06 December 2012; revision accepted 27 July 2013)

Abstract–Here, we report analyses by synchrotron X-ray fluorescence microscopy of the elemental composition of eight candidate impact features extracted from the Stardust Interstellar Dust Collector (SIDC). Six of the features were unambiguous tracks, and two were crater-like features. Five of the tracks are so-called "midnight" tracks—that is, they had trajectories consistent with an origin either in the interstellar dust stream or as secondaries from impacts on the Sample Return Capsule (SRC). In a companion paper reporting synchrotron X-ray diffraction analyses of ISPE candidates, we show that two of these particles contain natural crystalline materials: the terminal particle of track 30 contains olivine and spinel, and the terminal particle of track 34 contains olivine. Here, we show that the terminal particle of track 30, Orion, shows elemental abundances, normalized to Fe, that are close to CI values, and a complex, fine-grained structure. The terminal particle of track 34, Hylabrook, shows abundances that deviate strongly from CI, but shows little fine structure and is nearly homogenous. The terminal particles of other midnight tracks, 29 and 37, had heavy element abundances below detection threshold. A third, track 28, showed a composition inconsistent with an extraterrestrial origin, but also inconsistent with known spacecraft materials. A sixth track, with a trajectory consistent with secondary ejecta from an impact on one of the spacecraft solar panels, contains abundant Ce and Zn. This is consistent with the known composition of the glass covering the solar panel. Neither crater-like feature is likely to be associated with extraterrestrial materials. We also analyzed blank aerogel samples to characterize background and variability between aerogel tiles. We found significant differences in contamination levels and compositions, emphasizing the need for local background subtraction for accurate quantification.

INTRODUCTION

The twin goals of the Stardust mission were to capture, in separate collectors, particles from the coma of comet 81P/Wild 2, and particles from the interstellar dust stream flowing through our solar system (Grün et al. 1993). In this work, we focus on the captured contemporary interstellar dust candidates. Particles were collected on the interstellar dust collector of the spacecraft for a total exposure time of 229 days (Tsou et al. 2003). Aerogel tiles, designed to capture hypervelocity particles with minimal damage, were used as the primary collection medium. Critical components of the Stardust Interstellar Preliminary Examination (ISPE) project were to identify captured interstellar particles and to perform initial analyses of tracks and residual particles (Westphal et al. 2008). During the ISPE, only nondestructive analytical techniques were applied. At the same time, the expected small size of the particles requires analyses at the submicron scale. As a consequence, ISPE analyses rely heavily on synchrotron microprobe techniques (Westphal et al. 2010), including X-ray fluorescence (XRF), X-ray diffraction (XRD), scanning transmission X-ray microscopy (STXM), and Fourier transform infrared

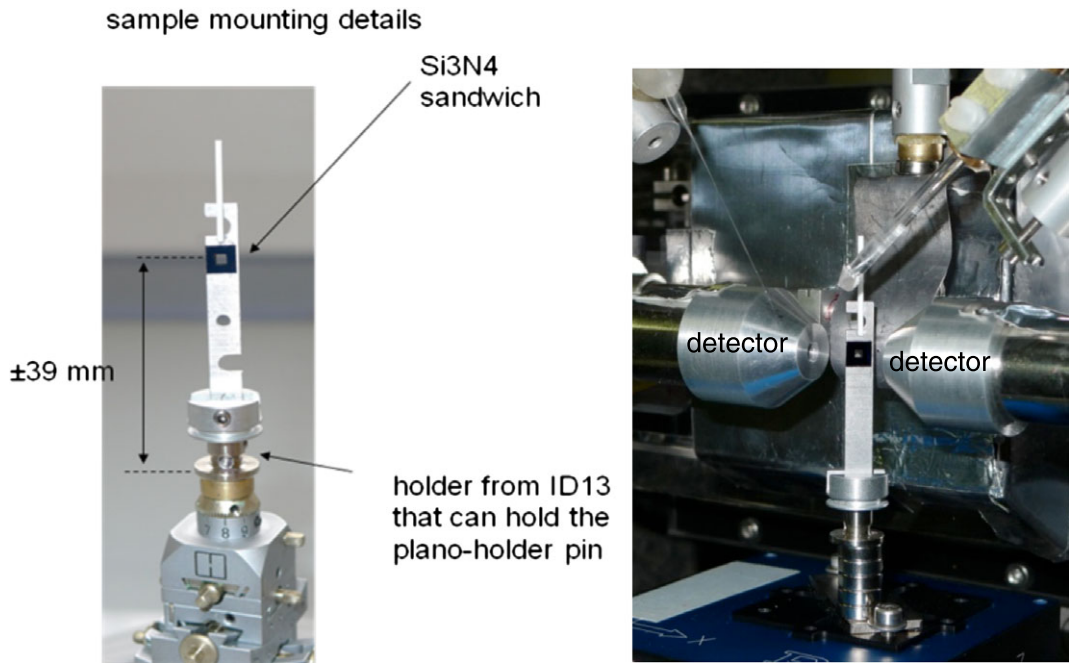

Fig. 1. (Left) Blue square surrounds the sample chamber—the picokeystone is sandwiched between two Si_3N_4 windows, the sample is mounted on a goniometer head; (Right) part of the experimental setup with two vortex detectors. Sample is on top of an x, y, z, θ nanocube motorized stage.

(FTIR) spectroscopy. Here, we present results from X-ray fluorescence (XRF) mapping and point analyses on interstellar candidates at beamline ID13 of the European Synchrotron Radiation Facility (ESRF).

XRF measurements are complementary to the other types of analyses conducted during the ISPE. Under these experimental conditions, the major limitation is that, among the major rock-forming elements in nature (C, O, Mg, Al, Si, S, Fe), XRF is sensitive only to S and Fe. This limitation is principally due to fluorescence of Si in the aerogel in which the particles are embedded, and to absorption in the aerogel and in the air path between the sample and the detector. A flow of He at the sample would have reduced the latter effect, but would have prevented XRF mapping at <200 nm resolution due to sample vibration. XRF is extremely sensitive to elements with $Z > 16$, and, with the use of appropriate standards, is highly quantitative and insensitive to systematic uncertainties due to local chemical bonding, as long as the beam energy is sufficiently high as compared with the energy of the X-ray absorption edge of the element under study.

METHODS

Sample Preparation

Sample preparation is described in detail in the companion paper by Frank et al. (2013). Here, we summarize the technique. Interstellar candidates were extracted from the interstellar collector in so-called picokeystones (Westphal et al. 2004; Frank et al. 2013). These wedge-shaped volumes of aerogel were machined from the aerogel collector tiles using glass needles controlled by automated micromanipulators. Unless otherwise noted below, the candidates were located in a thin (50–70 μm) section of the picokeystone, allowing all synchrotron-based analytical techniques to be applied without removing the particle(s) from the surrounding aerogel. The picokeystones were extracted on barbed polysilicon forks, then carefully sandwiched between two 70 nm thick Si_3N_4 windows. This mounting technique simultaneously protects the samples from contamination, reduces risk of loss by physically trapping the samples, and allows for nearly all synchrotron-based analyses.

XRF Measurements on Beamline ID13

The measurements presented here were performed at the nano-focusing beamline ID13 at the European Synchrotron Research Facility (ESRF). The experimental hutch is 90 m away from the source, which is a vacuum undulator optimized for 12.7 keV. The incident photon energy can be selected between 5 and 17 keV by means of a liquid N_2-cooled Si [111] double monochromator. The picokeystones were sandwiched between two Si_3N_4 windows, mounted on an Al plate (Fig. 1), and attached to a goniometer head.

This assembly is placed on a motorized stage (PI nanocube) that allows $x-$, $y-$, $z-$, and $\theta-$ movement on the nanometer scale. We measured the photon flux of the incident X-ray beam with an ionization chamber upstream of the sample. For the ID13 ISPE measurements, various focusing elements have been used, including a KB mirror or a Fresnel-lens system, producing an essentially symmetric submicron X-ray beam of 400 nm × 450 nm or 200 × 200 nm (H × V), respectively. The Fresnel focusing optics were designed and produced in the Laboratory for Micro- and Nanotechnology, PSI, Switzerland. High-resolution scanning was performed with step sizes of 100 or 200 nm to obtain high-quality two-dimensional XRF maps. Full spectra were acquired in each pixel. In addition, several high-quality point spectra were obtained on terminal particles and different hotspots along the impact tracks. For quantification, two glass standards, MPI-DING Atho-G and NIST SRM 612, were measured at the same location as the samples. Two energy-dispersive silicon drift detectors (VORTEX-EM SII NanoTechnology Inc., USA) were used in 90° geometry relative to the X-ray beam. The dual detector arrangement increases the XRF data collection efficiency by a factor of two.

Quantification Procedure

For ID13 data reduction, the first step of the spectral evaluation was performed using the AXIL software package (Vekemans et al. 1994) for elemental identification and the determination of the background-subtracted line intensities. Elemental maps were created with the MICROXRF2 software package, and were normalized with respect to the readout of the ionization chamber that was positioned in the beam path, close to the sample.

The actual quantification was carried out with long point measurements on strongly fluorescing points and on summed spectra that were created from the different maps. In the latter case, the spectra of the pixels that surround the particle were used to estimate the background contribution of the aerogel, which was subsequently subtracted from the summed spectra. This background subtraction approach has led to the removal of the Ar, Pb, Br, and Se (partial) signals from the spectra, indicating that the presence of these elements in the spectra cannot be attributed to the particle. While the Ar and Pb signals can be explained by the experimental conditions, the Br and Se signals are most likely due to the contamination of the aerogel, introduced during the manufacturing process, as already noticed by other investigators (Schmitz et al. 2009; Silversmit et al. 2010; Schoonjans et al. 2012).

The quantification model is based on the fundamental parameter method (Markowicz and Van Grieken 2001):

$$I_i = I_0 G w_i Q_i \varepsilon_i \Pi_{\text{exc}} \Pi_{\text{fluo}} \rho T A_{\text{corr}} \quad (1)$$

where I_i is the fluorescence background-subtracted line intensity of element i, I_0 is the intensity of the incident beam, G is the solid angle-dependent geometry factor, w_i is the weight fraction of element i in the layer of interest, Q_i is the production cross section of fluorescence photons for element i, ε_i is the detector efficiency for fluorescence photons for element i, Π_{exc} is the absorption of the excitation beam upstream of the sample, Π_{fluo} is the absorption of the fluorescence photons between the sample and the detector, ρ is the density of the layer of interest, T is the thickness of the layer of interest, and A_{corr} is the absorption correction for the layer of interest.

This equation was constructed for both sample (u) and a standard reference measurement (s), after which the ratio of both was observed

$$\frac{I_i^u}{I_i^s} = \frac{I_0^u \Pi_{\text{exc}}^u \Pi_{\text{fluo}}^u \rho^u T^u A_{\text{corr}}^u}{I_0^s \Pi_{\text{exc}}^s \Pi_{\text{fluo}}^s \rho^s T^s A_{\text{corr}}^s} \quad (2)$$

Several terms, such as the geometry factor and the XRF production cross sections, could be canceled out this way. This system of equations was subsequently solved for all elements i in an iterative manner, using a fundamental parameter software developed at the XMI group (Ghent University), yielding the weight fractions w_i. Schoonjans et al. (2012) give a full description of the exact algorithms.

The error estimation was performed using a Monte Carlo-based approach: we took the initial parameters (standard reference weight fractions, densities, spectra, particle dimensions, etc.) and varied them according to their corresponding standard deviations and measurement errors using Mersenne twister random-number generators (Matsumoto and Nishimura 1998) that spawned new parameters according to Poisson, uniform, or Gaussian distributions. These new parameters were subsequently used to obtain a new set of weight fractions w_i. Repeating this procedure several tens of thousands of times produces a reliable distribution of the standard deviations that are associated with the weight fractions (Schoonjans et al. 2012).

Below, we compare elemental concentrations measured in interstellar dust candidates with solar system abundances. For this purpose, we use tabulated CI meteoritic values given in Lodders and Fegley (1998). Except for volatile elements, CI abundances are

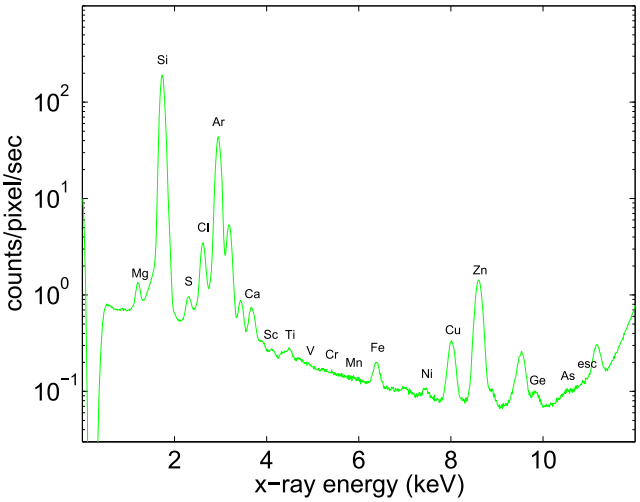

Fig. 2. Integrated X-ray fluorescence spectrum of a randomly chosen field of blank keystone I1013,1. Kα peaks are labeled. The incident X-ray energy was 13.8 keV.

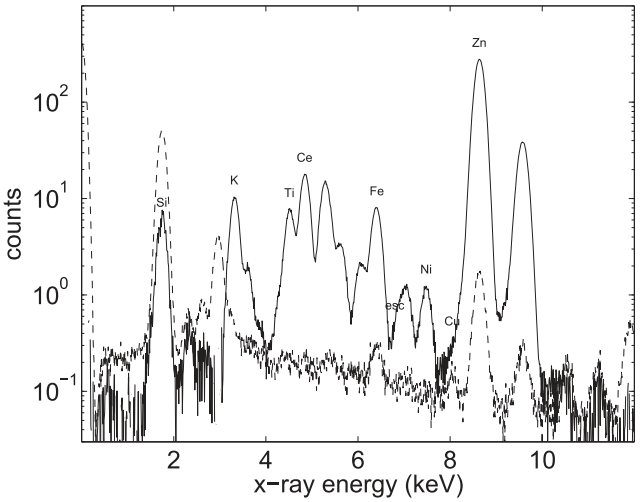

Fig. 3. Background-subtracted X-ray fluorescence spectrum of the terminal particle of I1017,2,1, showing the presence of abundant Zn and Ce. The background spectrum is shown as a dashed line.

thought to be representative of bulk solar system abundances. However, although bulk interstellar material probably has elemental abundances similar to those of the solar system, there is no reason a priori to expect individual interstellar dust particles to have the bulk composition, particularly if the number of discrete phases in the particles is small.

RESULTS

We performed analyses by synchrotron X-ray fluorescence microscopy of the elemental composition of eight candidate impact features extracted from the Stardust Interstellar Dust Collector (SIDC). Six of the features were unambiguous tracks, and two were crater-like features. An advantage of aerogel as a collection medium is its ability to passively record projectile trajectory (Burchell et al. 2012). Five of the tracks were so-called "midnight" tracks—impacts whose trajectory is consistent with an origin either in the interstellar dust stream or as secondaries from impacts on the Sample Return Capsule (SRC) (Westphal et al. 2014a).

Aerogel Backgrounds and Homogeneity

We evaluated backgrounds in all eight samples, as well as two blank keystones that were extracted for the purpose of measuring backgrounds and for process validation and rehearsal. As an example, in Fig. 2, we show the integrated XRF spectrum of the blank keystone I1013,1. Backgrounds were observed to be variable from sample to sample, but mostly homogenous within each sample. These backgrounds are presented as the green curves in the fluorescence spectra presented for each particle. Distinct hotspots in various elements, including Ca, Zn, Cr, and Fe, were occasionally observed, but these composed $\ll 10^{-4}$ of the area of most scans.

I1017,2,1

Track I1017,2,1 was observed in the Stardust SIDC with an azimuth angle $\phi = 58°$, indicating a probable origin as secondary ejecta from an impact on the port aft solar panel ($\phi = 0°$ is defined as the particle velocity vector pointing away from the SRC). The track was extracted in an ordinary keystone (Westphal et al. 2004), rather than a picokeystone. We collected XRF data (Fig. 3) with a 15.3 keV beam, focused to a spot of size between 200 and 300 nm. XRF analysis of the particle indicates abundant and highly correlated Ce and Zn (Fig. 4), which is consistent with the high-emissivity Ce-doped glass covering the spacecraft solar panels, and would be unexpected in natural extraterrestrial materials. The tricolor RBG (Ca, Zn, Ce) map shows that Ca is associated with the glass. However, Fe and Ni appear to be carried in a separate phase. Ni and Fe are well correlated in this phase, with a Ni/Fe ratio of approximately 0.1.

I1017,6,20

I1017,6,20 was a crater-like feature that we extracted in a picokeystone. Optical images taken from the side of the picokeystone after extraction indicated a very shallow feature on the surface. We analyzed this feature with a 14 keV beam. In Fig. 5, we show the

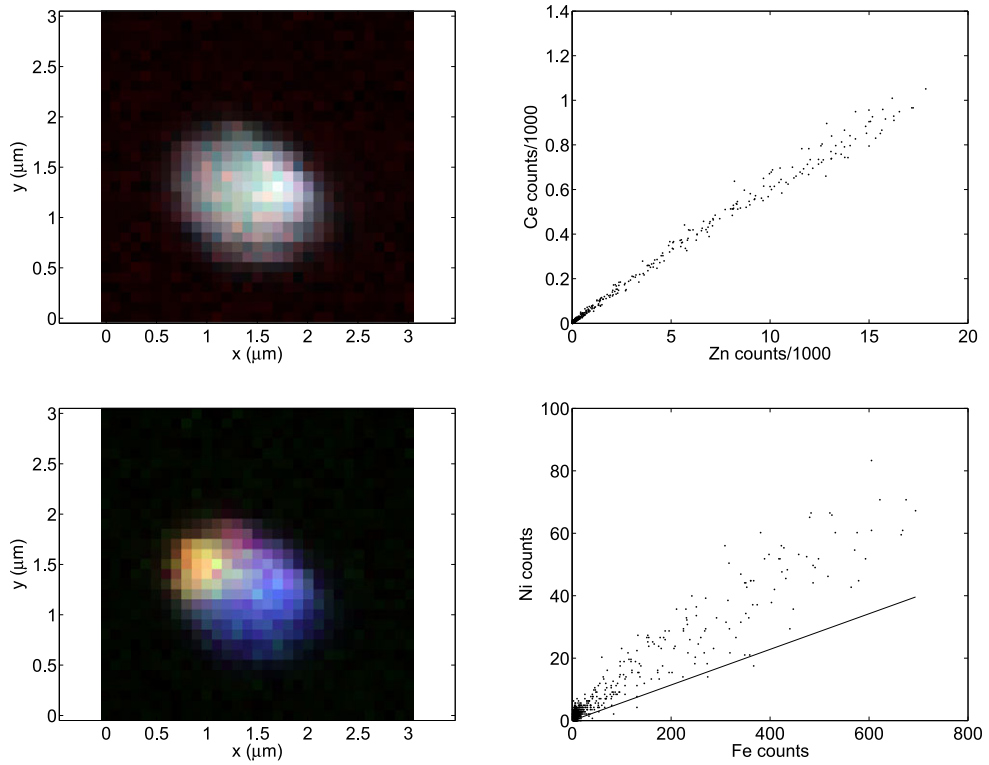

Fig. 4. Top left) Tricolor RGB (Ca, Zn, Ce) map of the terminal particle of I1017,2,1, indicating that Ca is associated with the spacecraft glass, and is unlikely to be a component of the primary impactor. The colors in each channel are normalized to the range of the concentration of the respective element. Top right) Pixel-by-pixel scatterplot of Zn versus Ce peak amplitudes. The data are uncorrected for absorption in the particle. Bottom left) Tricolor RGB (Fe, Ni, Zn) map of the terminal particle of I1017,2,1. The colors in each channel are normalized to the range of the concentration of the respective element. The (Fe,Ni)-bearing phase (yellow) appears to be distinct from the glass. Bottom right) Pixel-by-pixel scatterplot of Ni versus Fe peak amplitudes. The data are uncorrected for absorption in the particle, but are corrected for detection efficiency and fluorescence X-ray absorption cross sections. The CI Ni/Fe ratio is indicated by the black line.

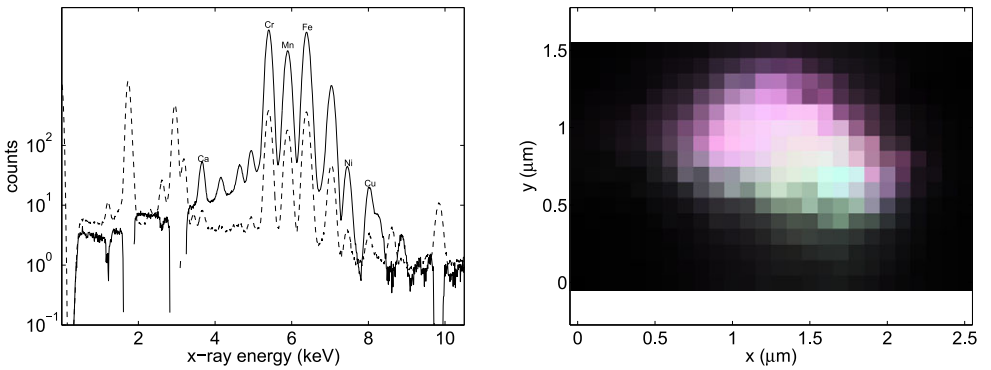

Fig. 5. Left) Background-subtracted X-ray fluorescence spectrum of the crater-like feature I1017,6,20. The background spectrum is shown as a dashed line. Right) Tricolor RGB (Fe, Cr, Mn) map of the crater-like feature of I1017,6,20. The colors in each channel are normalized to the range of the concentration of the respective element.

XRF spectrum, which shows weak Ni, and very large values of Cr/Fe, Mn/Fe, and Cu/Fe with respect to their CI values. The feature was sufficiently shallow that it appears unlikely to be a high-speed impact. While a cosmic origin cannot be ruled out based on its elemental composition, we did not pursue this particle further because of the low likelihood of an interstellar or interplanetary origin.

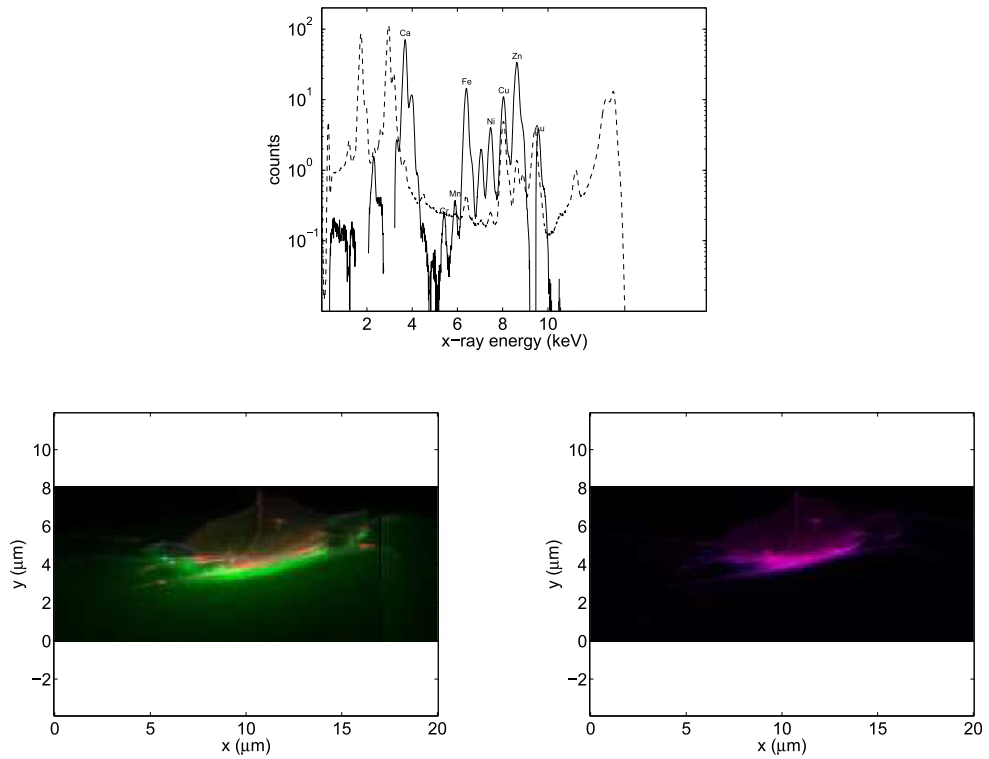

Fig. 6. Top) Background-subtracted X-ray fluorescence spectrum of the crater-like feature I1004,3,21. The background spectrum is shown in as a dashed line. Bottom left) Tricolor RGB (Ca, Cu, Zn) map of feature I1004,3,21. The colors in each channel are normalized to the range of the concentration of the respective element. Bottom right) Bicolor RB (Fe, Ni) map of feature I1004,3,21.

I1004,3,21

I1004,3,21 was an unusual, spider-like feature that showed crater-like features in the optical imagery. Examination from the side after extraction into a picokeystone showed that the object extended into the surface. In Fig. 6, we show the integrated XRF spectrum of this object. It shows extremely large enhancements in Ca/Fe, Cu/Fe, Zn/Fe, and Au/Fe with respect to CI values. The object appears to be a warped, possibly thin film with filament-like features, with enhanced, correlated Ca, Cu, and Zn. The aerogel under the object is Cu-rich, and the Cu appears to have diffused into the aerogel. Fe and Ni are present in the film-like structure, although Fe and Ni are correlated, there are variations in the Ni/Fe ratio. We conclude that this object is unlikely to have a cosmic origin, and is also unlikely to be an impact structure.

I1060,1,28

I1060,1,28 was a "midnight" track with a bilobate terminal particle. In Fig. 7, we show the integrated XRF spectrum of this object. The two lobes of the terminal particle are chemically distinct (Fig. 7). It shows extremely large enhancements in Cu/Fe and Zn/Fe with respect to CI values, so we conclude that this particle is unlikely to have a cosmic origin. However, the composition of track 28 is not consistent with samples taken from the SRC sample return capsule deck (Frank et al. 2013), so its origin is uncertain.

I1059,2,29 and I1092,1,37

I1059,2,29 and I1092,1,37 were both "midnight" tracks. The terminal particles in these tracks could not be located in XRF navigation scans, indicating that the heavy element concentrations in them were very low. Track 29 was subsequently identified as Al metal, and track 37 as glassy oxidized Al, consistent with an origin in the SRC deck, in STXM analyses (Butterworth et al. 2014). Measurements of samples taken from the deck of the SRC sample return capsule (Frank et al. 2013) indicate very small concentrations of heavy elements in this material.

I1043,1,30 (Orion)

Track 30 was named "Orion" by its discoverer, Bruce Hudson, on the Stardust@home project. Orion was one of the so-called "midnight" tracks, with a trajectory consistent with an origin either in the interstellar dust stream or as a secondary from an impact on the SRC. Track 30 was extracted in a

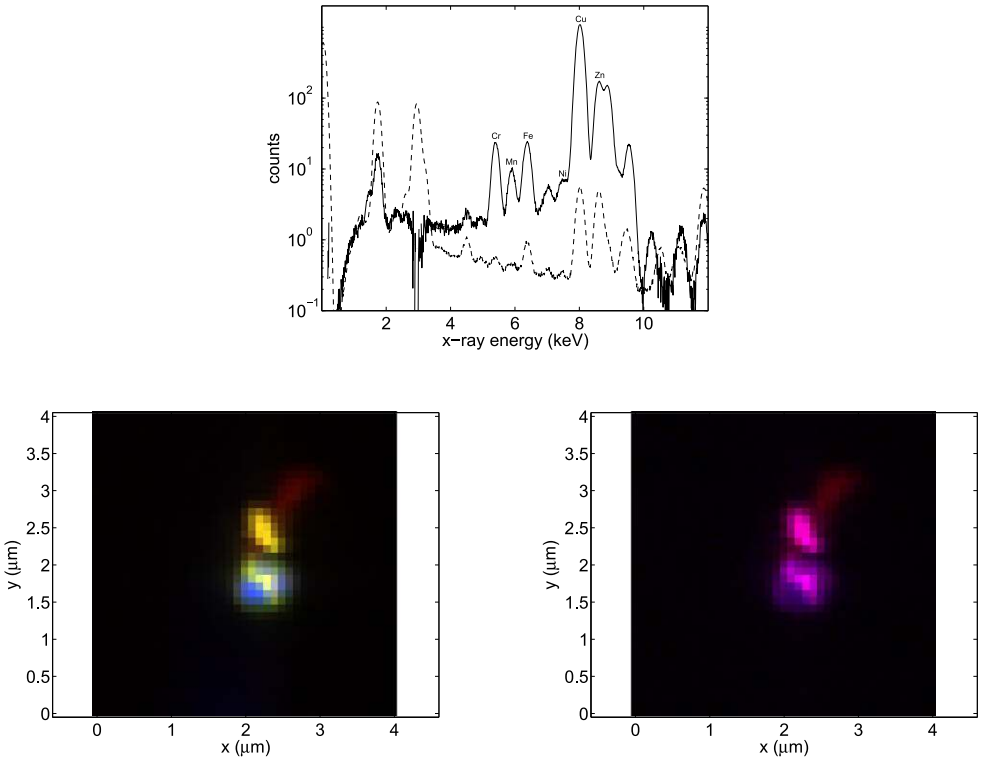

Fig. 7. Top) Background-subtracted X-ray fluorescence spectrum of the crater-like feature I1060,1,28. The background spectrum is shown as a dashed line. Bottom left) Tricolor RGB (Fe, Cu, Zn) map of feature I1060,1,28. The colors in each channel are normalized to the range of the concentration of the respective element. Bottom right) Bicolor RB (Fe, Ni) map of feature I1060,1,28.

picokeystone. We collected XRF and XRD data on the terminal particle on beamline ID13, using a 13.8 keV beam. In Fig. 8, we show optical images of track 30 taken just after extraction in the Curatorial Facility at Johnson Space Center, and on the beamline at ID13.

Figure 9 shows the first XRF map taken of Orion that resolves its internal structure. We also note the absence of the particle ("Sirius") identified in subsequent analyses just to the left of the Orion (Butterworth et al. 2014). The implications of this observation are discussed in companion papers by Butterworth et al. (2014) and Simionovici et al. (2014). In Figs. 9–15, the maps are flipped vertically in order to consistent in orientation with the STXM maps reported in Butterworth et al. (2014).

Figure 10 shows background-subtracted summed XRF spectrum for Orion, as well as the background spectrum. Derived elemental masses for Orion are given in Table 1. In Table 2, we summarize the derived elemental ratios for the various scans, normalized to Fe.

Fe and Ni are correlated in Orion, with an average atomic ratio close to the chondritic value (Fig. 11). However, Fe and Ni reside in two separate phases with different Ni/Fe ratios. The low-Ni region may correspond to the olivine phase observed in the XRD topographs (Gainsforth et al. 2014).

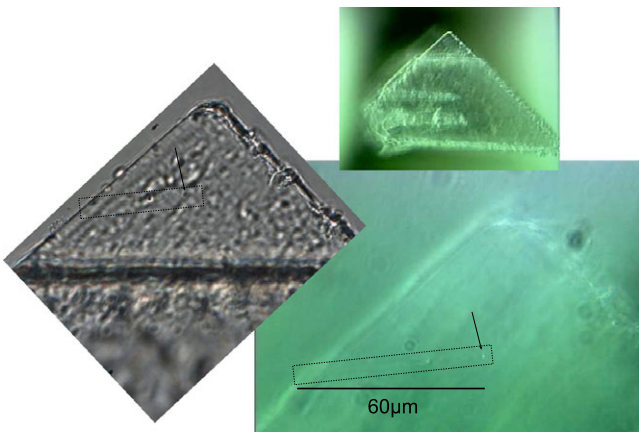

Fig. 8. Left) JSC photodocumentation of track 30 immediately after extraction from the collector tray. Top right) Low-magnification image of the track 30 picokeystone at ID13. Bottom right) High-magnification image of track 30. Dashed boxes outline the track, and arrows indicate the terminal particle, Orion.

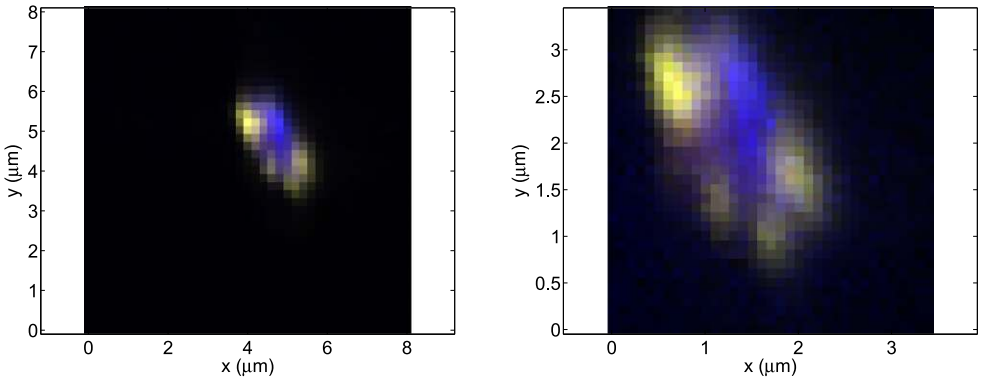

Fig. 9. Left) Tricolor RGB = (Fe, Ni, Ca) moderate-resolution (200 nm) map (scan 299) of Orion, showing the presence of only one terminal particle within this field of view. The particle Sirius, discussed by Butterworth et al. (2014) in STXM and subsequent analyses, would be expected at (x, y) = (2 μm, 5 μm). The colors in each channel are normalized to the range of the concentration of the respective element. Right) Tricolor RGB = (Fe, Ni, Ca) high-resolution (100 nm) map of Orion, showing more detailed internal structure in Orion.

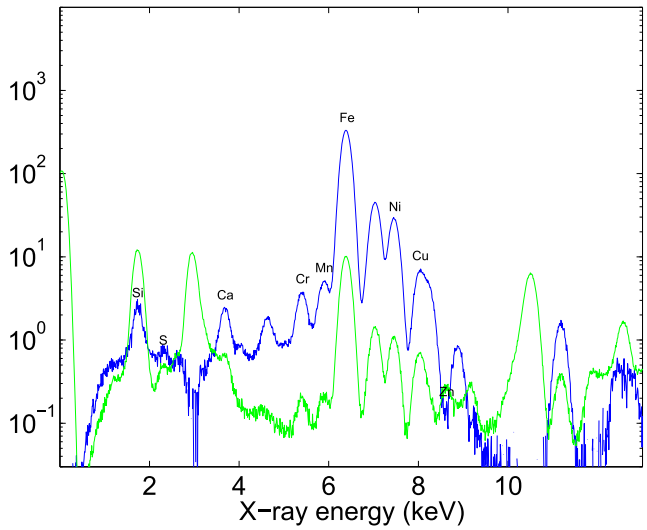

Fig. 10. Scan 299 background-subtracted integrated XRF spectrum of Orion (upper) and background spectrum (lower).

Cr and Mn (Fig. 12) are distributed in a large, nearly homogenous area that subtends the map of Orion in all elements. Cr and Mn are well correlated, but with some scatter, perhaps reflecting the apparent zoning, with the Cr/Mn ratio increasing toward the edge of the region. Ca appears to be associated with this phase, although it is not homogeneously distributed (Fig. 13).

We also investigated possible correlations among S, Fe, and Cu (Fig. 14). We identify at least two grains in which Cu and Fe are well correlated, with atomic Cu/Fe ratios of approximately 0.040 and 0.022, respectively (Fig. 15). Minor S, correlated with Fe, is also present in Orion (Fig. 15, right), with S/Fe approximately 0.04 (atomic).

Table 1. Summary of analyses of elemental mass measurements for three scans. With the exception of S, statistical errors are negligible; absolute errors are dominated by systematic uncertainties, which are of order 10%. The tabulated values for Si were Si associated with Orion, but we cannot distinguish Si from melted and compressed aerogel around the particle from Si native to the particle, so this should be treated as an upper limit.

	Mass (fg)		
	Scan 299	Scan 300	Scan 301
Si*	1743*	1768*	1740*
S	23	16	12
Ca	16	14	14
Cr	12	11	11
Mn	14	12	12
Fe	840	790	780
Ni	55	51	51
Cu	11	10	10

*Includes melted and compressed aerogel.

Table 2. Summary of analyses of elemental abundances for four scans.

	Atomic fraction (%) (Fe ≡ 100)		
	Scan 299	Scan 300	Scan 301
Ca	3.77 ± 0.12	3.54 ± 0.11	3.57 ± 0.12
Cr	1.53 ± 0.05	1.58 ± 0.05	1.59 ± 0.05
Mn	1.69 ± 0.05	1.65 ± 0.05	1.66 ± 0.05
Ni	6.17 ± 0.24	6.14 ± 0.24	6.16 ± 0.24
Cu	1.15 ± 0.06	1.15 ± 0.06	1.12 ± 0.06

To summarize, based on XRF measurements, Orion appeared to consist of a 2 μm by 1 μm, nearly

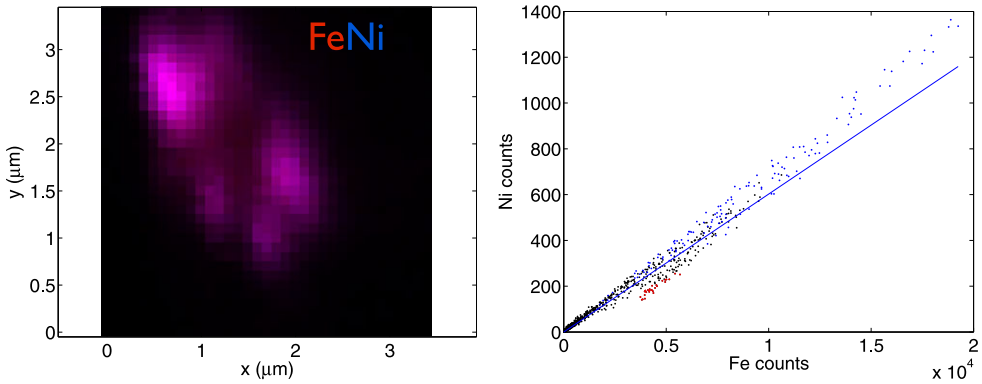

Fig. 11. Left) Scan 299 bicolor Fe (red) Ni (blue) map. The center of the particle, weakly visible in red, is low in Fe and Ni, and shows a smaller Ni/Fe ratio than the Fe,Ni-rich peripheral grains. Right) Pixel-by-pixel correlation between Fe and Ni. Blue points correspond to peripheral grains; red points correspond to points near the center of the particle, well separated from peripheral grains; black points are all other points. The blue line corresponds to the average Ni/Fe atomic ratio in Orion, 6.5%.

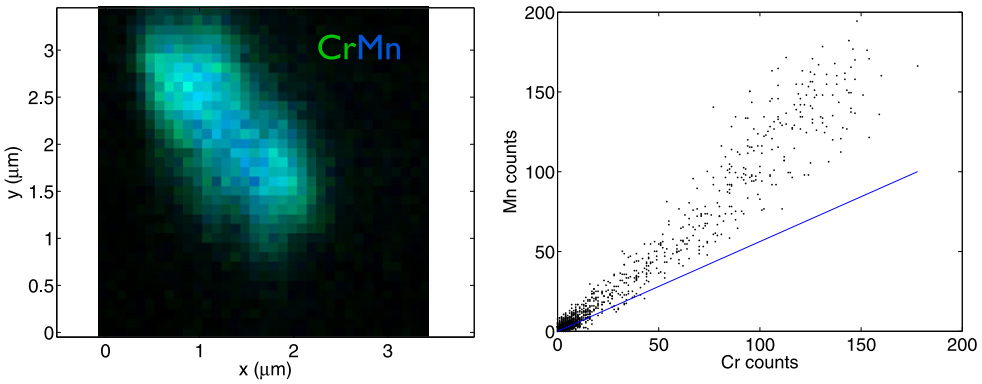

Fig. 12. Left) Scan 299 bicolor GB (Cr, Mn) map. Right) Pixel-by-pixel correlation between Cr and Mn. The black line corresponds to the CI value, 0.71.

homogeneous Fe-bearing grain, surrounded by four submicron, Fe-rich grains that contain minor Ni, S, and Cu. We emphasize that this analysis is based only on the analysis of elements that are detectable by this technique. STXM (Butterworth et al. 2014) and XRD (Gainsforth et al. 2014) analyses indicate the presence of spinel. The diversity of the Cu/Fe ratio in these particles may indicate that they formed in diverse environments and were later incorporated into Orion. Correlation of these maps with XRD topographs (Gainsforth et al. 2014) and STXM (Butterworth et al. 2014) analyses led to the conclusion that the mineralogy of this grain is consistent with olivine, and is likely to be the particle named "Sirius" identified in subsequent STXM (Butterworth et al. 2014) and XRF analyses (Simionovici et al. 2014). In this phase, Cr/Fe and Mn/Fe are above chondritic values and the Ni/Fe ratio is below the chondritic (Fig. 11); Ca, Cr, and Mn contents are consistent with the values in chondritic olivines (Brearley and Jones 1998) and Wild 2 olivines (Joswiak et al. 2012). We estimated an upper limit on the mass of Fe in the olivine particle to be approximately 400 fg, by taking the lowest value of Fe/Cr observed near the center of the particle image, as

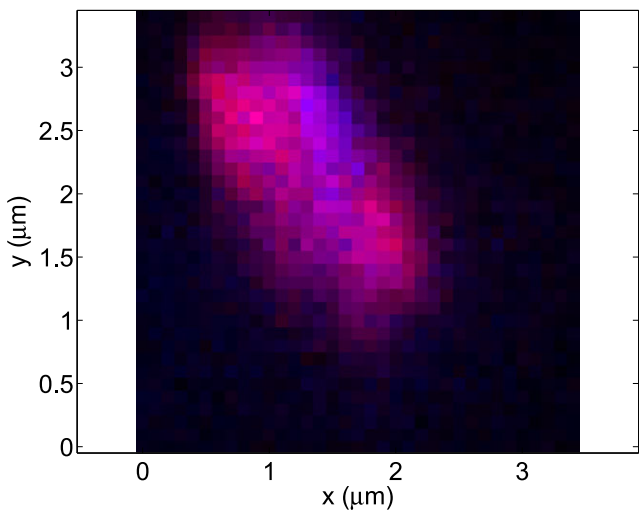

Fig. 13. Scan 299 bicolor RB (Cr, Ca) map.

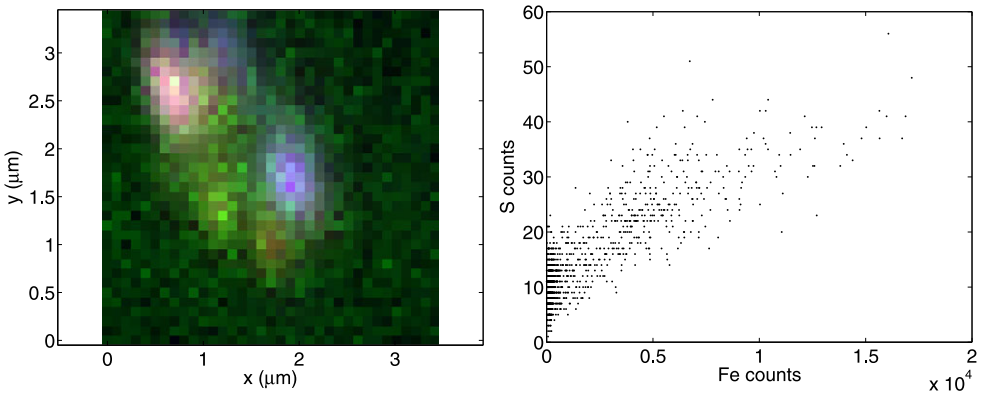

Fig. 14. Left) Scan 299 tricolor Fe (red) S (green) Cu (blue) map. Right) Pixel-by-pixel correlation between Fe and S.

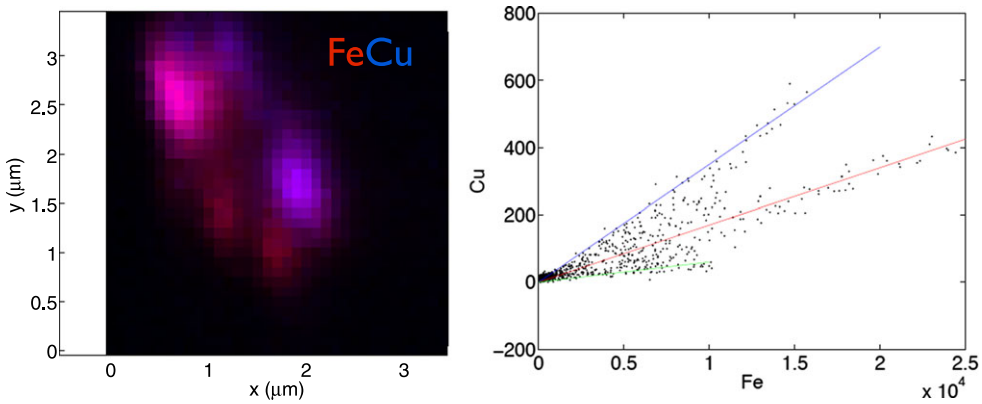

Fig. 15. Pixel-by-pixel correlation between Fe and Cu.

far as possible from the peripheral grains, as representative. Taking the Mg mass of 300 fg as measured on STXM, we find that the forsteritic content of the olivine is $Fo_{>60}$, with approximately 0.5 wt% Ca, Cr, and Mn. Evidence from ID22 (Gainsforth et al. 2014; Simionovici et al. 2014) and STXM (Butterworth et al. 2014) suggests that the fayalitic content is much lower, with most of the Fe present in different phases.

I1047,1,34 (Hylabrook)

Track 34, Hylabrook, was named by its discoverer, Naomi Wordsworth, a volunteer on the Stardust@home project (Westphal et al. 2014b). Like Track 30, Track 34 was a midnight track with a trajectory consistent with either an origin in the interstellar dust stream, or as secondary ejecta from the SRC. We extracted track 34 in a picokeystone, and collected XRF and XRD data on the terminal particle on beamline ID13, using a 13.8 keV beam and a 200 nm by 200 nm beamspot. The XRD analyses are presented in the companion paper by Gainsforth et al. (2014). In Fig. 16, we show the (Fe, Ni) map of the Track 34 terminal particle Hylabrook.

We derived a total Fe mass of 1300 ± 100 fg in Hylabrook. In Fig. 17, we show the integrated XRF spectrum after background subtraction, as well as the background spectrum, and in Table 3, we report elemental atomic ratios.

In Fig. 18, we investigate the correlation among Fe, Cr, and Mn, the three major elements detected by XRF in Hylabrook. Cr and Fe are weakly correlated, and zoning is evident in Cr/Fe across the particle. The correlation between Mn and Cr is stronger than between Cr and Fe.

In Fig. 19, we show the derived elemental abundances of Hylabrook, normalized to the Mg abundance measured by STXM (Butterworth et al. 2014) and CI.

Assessment of Possible Radiation Effects Due to ID13 Analysis

Tracks 30 and 34 underwent changes during the course of the ISPE. These are described in more detail in the companion STXM paper (Butterworth

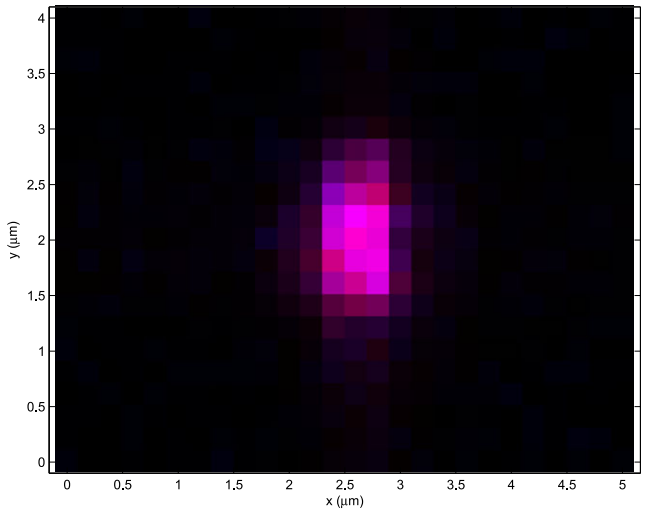

Fig. 16. Left) Bicolor Fe (red), Ni (blue) map of Hylabrook, the terminal particle of Track 34.

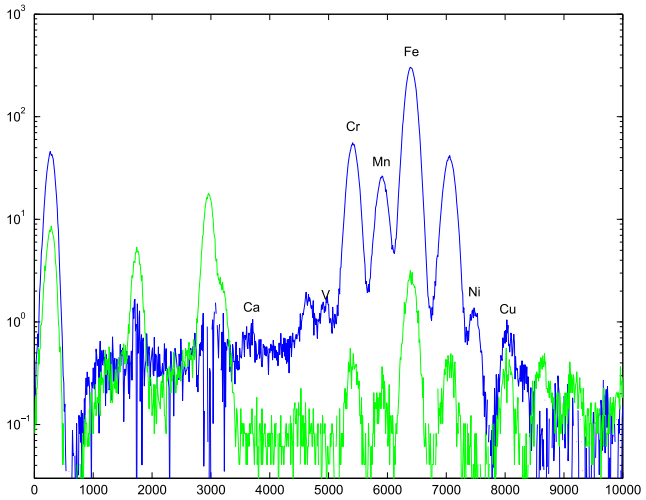

Fig. 17. Background-subtracted X-ray fluorescence spectrum of the terminal particle of track 34 (Hylabrook) (upper curve). The background spectrum is shown by the lower curve.

Table 3. Analysis of minor heavy elements in two scans on Hylabrook.

	Atomic fraction (%) (Fe ≡ 100)	
	Scan 173	Scan 176
Ca	0.85 ± 0.11	0.58 ± 0.09
Cr	29.9 ± 2.0	24.7 ± 1.8
Mn	8.7 ± 0.6	8.2 ± 0.6
Ni	0.28 ± 0.02	0.28 ± 0.02
Cu	0.17 ± 0.01	0.15 ± 0.01

et al. 2014). In view of these changes, we assess the possibility that analyses at ID13 were responsible for the observed changes. We treat the two tracks separately.

Track 30

Butterworth et al. (2014) report on STXM analyses of Track 30 performed following the ID13 analytical run. The STXM analyses were carried out at normal incidence, while the ID13 analyses were performed with at an incidence angle of 45° to the face of the picokeystone. STXM analyses show the presence of two particles at the terminus of the track: Orion, which was a fine-grained object with a shape similar to the terminal particle of track 30 as observed by ID13, and Sirius, which was observed to be approximately 3 μm upstream of Orion. We also observed a crack-like feature approximately 15 μm from the end the track, and also observed an enhanced optical density in the aerogel, in a diffuse, broad line centered on Orion, and extending approximately 40 μm on either side of it, consistent with a beam at 45° incidence angle centered on Orion. STXM analysis of Orion showed 425 ± 25 fg of Al, 200 ± 40 fg of Mg, and 12–20 fg of Fe. Mg and Al XANES data were consistent with spinel. Subsequent XRD analysis on ESRF beamline ID22 (Gainsforth et al. 2014) was also consistent with spinel, but, in contrast with the ID13 analysis, there were no diffraction spots that were consistent with olivine. Sirius consisted of an amorphous, Mg-rich phase, with 300 ± 60 fg of Mg. Subsequent STXM (ALS 11.0.2) and SXRF (ESRF ID22) analyses show the presence of Mg and Fe in the track and the crack, and approximately 1 fg of Fe and approximately 4 fg of Ni in Sirius. We also detected diffuse Fe, with a total mass of 800 ± 100 fg, in the aerogel around the track. The conclusion of the STXM analyses is that, following the initial ID13 analysis, approximately 97% of the Fe in the original Orion particle had moved down the track, into a newly formed crack in the aerogel, and had diffused into the surrounding aerogel. Furthermore, a particle that may have been consistent with the large, homogenous olivine-like feature described above (Fig. 12) had separated from the terminal particle and had been amorphized to become Sirius.

To investigate the possibility of beam damage and loss of Fe from Orion during our analyses, we measured the Fe mass in Orion for several scans. These scans included the first high-resolution scan of Orion (scan 261), and also include the last map done of the entire track (scan 308). In Fig. 20, we show the Fe mass in Orion as a function of scan number. We see no indication of loss of Fe during these scans. We particularly point to scans 302 and 303, which were the highest resolution, longest dwell scans. The scan was interrupted in the middle of scan 302, and resumed to complete the scan of the particle in scan 303. Because of vertical drift during this scan, the measured Fe mass was larger than seen in the other, faster scans.

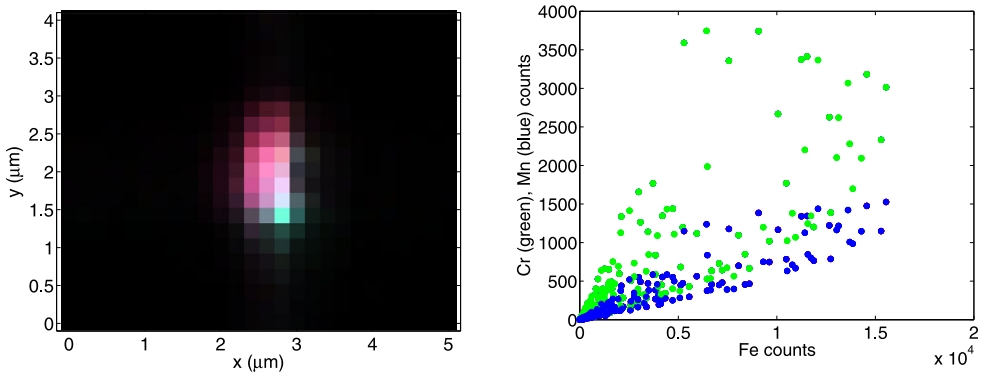

Fig. 18. Left) Tricolor Fe (red) Cr (green) Mn (blue) map. Right) Pixel-by-pixel correlation between Fe and Cr. The colors in each channel are normalized to the range of the concentration of the respective element.

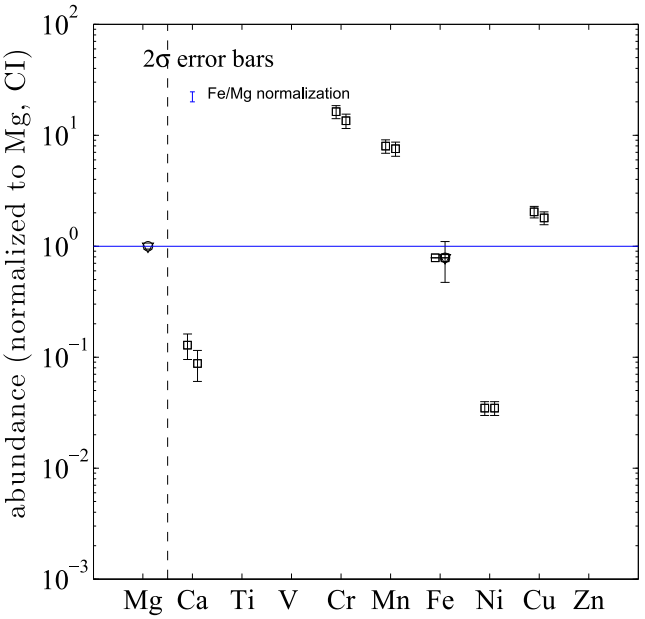

Fig. 19. Abundances of elements in Hylabrook, normalized to Mg and CI, for scans 173 and 176. The 2σ error on the overall Fe/Mg normalization between XRF and STXM measurements is indicated by the blue error bar.

Nevertheless, in scan 308, which was performed subsequently, we see no change in the morphology or Fe mass of Orion, and, in particular, we see no evidence for the existence of Sirius.

We considered the possibility of inadvertent, undocumented beam damage after scan 308, but before the termination of the run and unloading of the sample. We can rule out, beyond a reasonable doubt, that an intense, white or pink beam entered the experimental hutch. This is not possible by mechanical design, because of a fixed white beam beamstop, and a 12.5 mm offset between the white beam and the monochromatic beam. Such an event would not be consistent with dosimeter recordings, which would see the Brehmstrahlung radiation. Furthermore, we did not observe any other effects to be expected from such an event, such as destroyed Kapton windows, mirrors, or loss of vacuum.

Concerning the monochromatic beam, the beam intensity is close to the maximum possible on this beamline. There are primary and secondary slits that can be opened to a maximum of 700 μm by 700 μm. Furthermore, the ID13 beam is prefocused via a set of Be-CRL lenses in the white beam, which can be regarded as a fixed effective aperture of 900 μm in general, and less than 700 μm at 14 keV and lower energies. Finally, there is a set of beam-defining slits (BDS) in front of the final stage focusing optics, which is adapted to the aperture of the focusing device, with a maximum opening of 200 μm by 200 μm. This pair of slits limits the exposure of the optics in case the upstream slits are inadvertently opened. If the BDS were accidentally opened, this would have increased the intensity by, at most, a factor of two, and this would mostly increase the far beam tails instead of contributing to the flux density in the center of the spot. This is because the increased beam would not be focused properly and would mostly have been caught by the 20 μm guard aperture, which is installed near the focal spot.

Track 34, Hylabrook

In contrast with track 30, Track 34 was analyzed by STXM before analysis on ID13. STXM observations of Hylabrook before ID13 analysis show an approximately 1 μm, Mg-rich object with a Mg-XANES spectrum consistent with olivine, and low Fe, consistent with forsteritic olivine. STXM observations of Hylabrook after the ID13 measurements show the formation of an extended halo, approximately 3 μm in diameter. The Mg-XANES spectrum of the halo is similar to the pre-ID13 STXM analyses, indicating that the effect on Track 34 was mostly a mechanical disruption, rather

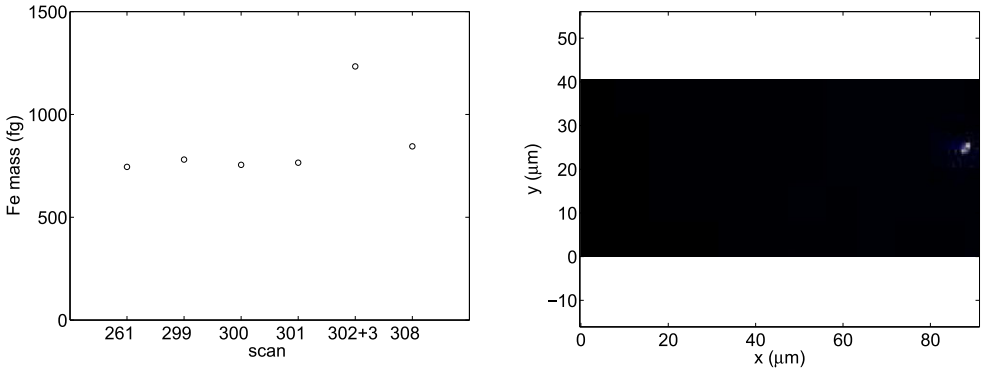

Fig. 20. Left) Measured mass in Orion as a function of scan. Scan 261 is the first high-intensity scan of the run, and scan 308 is the last. Right) Tricolor RGB (Fe, Ni, Ca) map of track 30. Scan 302 + 3 experienced vertical drift during the analysis, leading to an artificially high derived Fe mass. The track extends from x = ~0 μm to the position of the terminal particle Orion at x = 90 μm.

than a chemical or mineralogical change. The ID13 analysis exceeded the self-imposed fluence limits, derived from estimates of the astrophysical radiation dose (Gruber et al. 1999) experienced by interstellar particles, by approximately two orders of magnitude. Even so, here we observe a relatively minor effect on the terminal particle, and we observed no effect on the absorption characteristics of the aerogel.

Based on the evolution of Fe and lack of change in morphology of Orion and Hylabrook during the XRF/XRD analyses, we conclude that hard X-ray microprobe analysis is safe for analysis of small particles in aerogel, as long as analysis fluxes and fluences are maintained below reasonable limits, as described in Butterworth et al. (2014). We have assessed the possibility of X-ray analysis as a source for the loss of Fe and disruption of Orion, and so far have not identified any plausible mechanism. We have drawn a similar conclusion in the case of the STXM analysis (Butterworth et al. 2014) and so conclude that the cause of the disruption of Orion may lie somewhere other than in the synchrotron analyses. Future work on analogs in aerogel may resolve this mystery. Regardless, the multiple successive maps on Orion show that high-quality XRF and XRD data can be obtained without modification of the particle. This demonstrates that the damage events we experienced were not an inherent consequence of normal synchrotron activities, but were due to an uncontrolled and undocumented event of unknown origin. This is a very important distinction and shows that hard nano-XRF analyses can be safe.

DISCUSSION

In a companion paper reporting synchrotron X-ray diffraction analyses of ISPE candidates, we show that two of these particles contain natural crystalline materials:

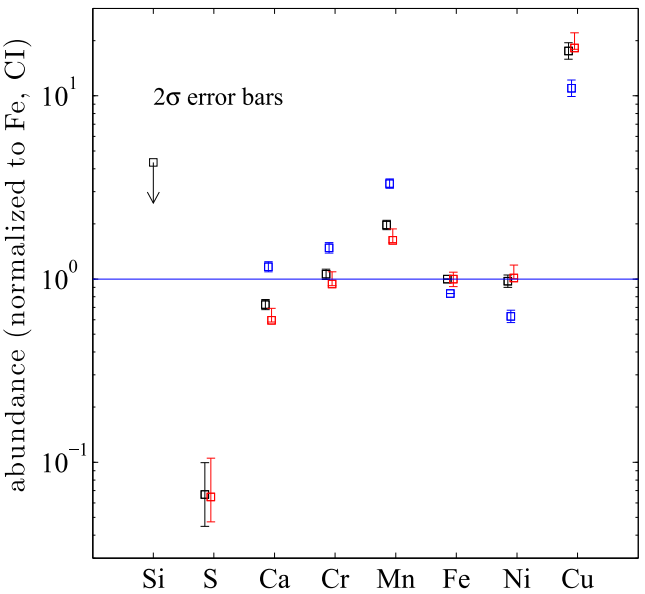

Fig. 21. Abundances of elements in Orion, normalized to the average Fe column density, and to CI. The black points are the entire particle, the red points are the peripheral submicron Fe-rich grains, and the blue points are points near the center of the particle that appear to be clear of peripheral grains.

the terminal particle of track 30 contains olivine and spinel, and the terminal particle of track 34 contains olivine. Of the eight candidate impact features that we analyzed, two, Tracks 30 (Orion) and 34 (Hylabrook), are dominated by extraterrestrial materials. In these analyses, we detected no obvious anthropogenic materials. Both of these features have their trajectories that are consistent with an origin either in the interstellar dust stream, or as secondaries from impacts on the SRC lid.

In Fig. 21, we show the results of the elemental abundances of Orion, normalized to Fe and to CI.

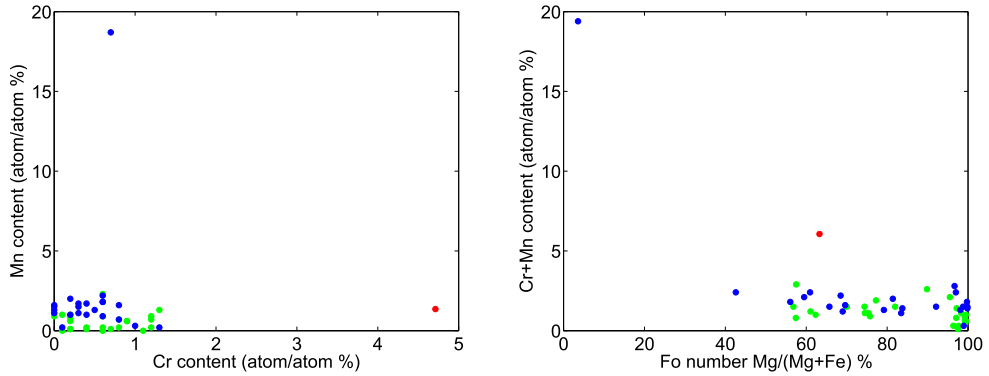

Fig. 22. Left) (Cr + Mn) versus forsteritic content and (right) Cr versus Mn content for chondritic olivines (green) (Brearley and Jones 1998), Wild2 olivines (Joswiak et al. 2012), and Hylabrook (red).

Summing the masses of the measurable components, including the measurements of the masses of Al and Mg from the STXM analyses, and estimating the volume of Orion assuming that it an ellipsoid, with the hidden dimension, parallel to the X-ray beam, taken to be the geometric mean of the other axes, we estimate a density of approximately 0.7 g cm^{-3} for Orion if the Si associated with Orion is included, and approximately 0.4 g cm^{-3} if the Si is assumed to be associated with a cap of compressed aerogel.

In the peripheral Fe-rich grains, the Ni/Fe ratio is approximately 20% higher than chondritic; Cr and Mn are depleted by at least a factor of five. At least half of the Fe is in the peripheral grains. We consider two possibilities for this phase.

Based on the presence of S and Cu, a chalcophile element often associated with sulfides, we first consider the possibility that these grains are heated and decomposed sulfides, and now consist of Fe metal with minor residual S (when the S fugacity is low, Cu resides entirely in metal [Humayun, personal communication]). However, we found no diffraction spots or rings consistent with metal (Gainsforth et al. 2014), but it is possible these might not be seen if the grains were monocrystalline and oriented unfortuitously. The S/Fe ratio is far below that of stoichiometric sulfides, so if this is the case, S was lost during capture in the aerogel or previously, perhaps as a result of processing in the interstellar medium prior to capture. In the XRD analyses, only one diffraction spot is a weak match for sulfide. An unidentified crystalline phase reported by Gainsforth et al. (2014) is also weakly consistent with a sulfate, which raises the possibility of terrestrial weathering of sulfides before the analysis. However, the low S/Fe ratio in Orion appears to be inconsistent with this hypothesis. Furthermore, the unidentified phase is equally consistent with many other minerals with unit cell ≥8 Å. Small (approximately 20 nm) metal particles surrounded by sulfide rims are ubiquitous in the Stardust cometary samples (Ishii et al. 2008). Leroux et al. (2009) interpret these as the product of sulfides, which were heated during capture, lost S into the gas phase, forming metal beads, which then reacted with the S gas during cooling, forming the sulfide rims. This process occurred within a much larger volume of heated material. On the other hand, observations of ≫1 μm sulfide grains decelerating in aerogel show evidence for melting and shedding of sulfide droplets along the tracks, rather than decomposition of sulfides. This observation tends to favor a scenario in which S was lost before capture, if the peripheral particles were originally dominantly sulfides.

Based on the weak association of the location of the peripheral grains with the spinel phases in the XRD topographs (Gainsforth et al. 2014), we also consider the possibility that the Fe-rich peripheral particles were a form of spinel. This hypothesis is consistent with Fe L-edge XANES (Butterworth et al. 2014) measurements, which indicate that the Fe in at least three of these particles is in the 2+ state (the largest peripheral particle was lost between the ID13 analysis and the first STXM analysis). However, the source of a correlation of S with spinel, which is not a host for this element, is difficult to explain in this scenario.

XANES (Butterworth et al. 2014) and XRD (Gainsforth et al. 2014) analyses of Hylabrook are both consistent with olivine mineralogy. In Fig. 19, we show the results of the analyses of Hylabrook, normalized to Mg from the STXM measurement (Butterworth et al. 2014) and CI, and on the assumption that no phases other than olivine are present; in Fig. 22, we compare the forsteritic content of Hylabrook with a compilation of measurements of olivines in chondritic meteorites, and with measurements of olivines from comet Wild2. The relatively large concentration of Cr in Hylabrook is reminiscent of so-called LICE (low-iron, chromium-enhanced) and LIME olivines, which may be the

product of primary condensation (Klöck et al. 1989). Ebel et al. (2012) have recently investigated the conditions in which LIME olivines form and are stable, and found that highly reducing conditions are required. Although they did not specifically model the incorporation of Cr into olivine, they predicted that the behavior of Cr would be qualitatively similar, and that Cr would be less readily incorporated into olivines during primary condensation. However, the large abundance of Cr observed in Hylabrook is too large to be consistent with LICE olivine, which can host a maximum of approximately 1.5% Cr, so the Cr must reside in a different phase, perhaps chromite or in an amorphous phase.

CONCLUSION

Because energy-dispersive fluorescence detectors for XRF and diffraction cameras for XRD can usually be used simultaneously on synchrotron hard X-ray microprobes, both types of analyses can be carried out without increasing the integrated X-ray fluence on samples. XRF data, presented here and in companion papers (Flynn et al. 2014; Simionovici et al. 2014), are complementary to FTIR (Bechtel et al. 2014), XRD (Gainsforth et al. 2014), and STXM (Butterworth et al. 2014) analyses. Data presented here have allowed us to identify secondary ejecta and anthropogenic contaminants with a high degree of confidence, and to characterize the distribution of minor heavy elements in particles that have been identified by other techniques as being of probable extraterrestrial origin. Because of our general ignorance of the properties of individual interstellar dust grains, we are not yet able to interpret these data so as to place these particles in an astrophysical context. This is hardly surprising as, prior to these same particles, no interstellar dust particles from the local interstellar medium have been available for study. As described in Westphal et al. (2014a), these interpretations will require further detailed study, including confirmation of interstellar origin by isotopic analyses. Although some questions remain, we have demonstrated that synchrotron hard X-ray analyses can be conducted with little risk to the samples, if adequate precautions against exceeding fluence limits are taken.

Acknowledgments—This manuscript was improved due to the thoughtful comments of John Bradley. The ISPE consortium gratefully acknowledge the NASA Discovery Program for Stardust, the fourth NASA Discovery mission. AJW, ALB, ZG, RL, DZ, WM, and JVK were supported by NASA grant NNX09AC36G. We thank Steve Boggs for astrophysical soft X-ray spectra. RMS, HCG, and NDB were supported by NASA grant NNH11AQ61I. The Advanced Light Source is supported by the Director, Office of Science, Office of Basic Energy Sciences, of the U.S. Department of Energy under Contract No. DE-AC02-05CH11231. Use of the National Synchrotron Light Source, Brookhaven National Laboratory, was supported by the U.S. Department of Energy, Office of Science, Office of Basic Energy Sciences, under Contract no. DE-AC02-98CH10886. We like to thank the ESRF for the allocated beamtime at ID13, instrumental and technical support. FEB and SS were supported by funding of the German Science Foundation (DFG).

Editorial Handling—Dr. John Bradley

REFERENCES

Bechtel H. A., Gainsforth Z., Brenker F. E., Burghammer M., Simionovici A., Schmitz S., Cloetens P., Lemelle L., Sans Tresseras J., Schoonjans T., Silversmit G., Solé V. A., Vekemans B., Vincze L., Westphal A. J., Allen C., Anderson D., Ansari A., Bajt S., Bastien R. S., Bassim N., Borg J., Bridges J., Brownlee D. E., Burchell M., Butterworth A. L., Changela H., Davis A. M., Doll R., Floss C., Flynn G., Frank D., Grün E., Heck P. R., Hillier J. K., Hoppe P., Hudson B., Huth J., Hvide B., Kearsley A., King A. J., Lai B., Leitner J., Leroux H., Leonard A., Lettieri R., Marchant W., Nittler L. R., Ogliore R., Ong W. J., Postberg F., Price M. C., Sandford S. A., Srama R., Stephan T., Sterken V., Stodolna J., Stroud R. M., Sutton S., Trieloff M., Tsou P., Tsuchiyama A., Tyliszczak T., Korff J. V., Wordsworth N., Zevin D., Zolensky M. E., and >30,000 Stardust@home dusters. 2014. Stardust Interstellar Preliminary Examination III: Infrared spectroscopic analysis of interstellar dust candidates. *Meteoritics & Planetary Science*, doi:10.1111/maps.12125.

Brearley A. J. and Jones R. H. 1998. Chondritic meteorites. In *Planetary materials*, edited by Papike J. J. Reviews in Mineralogy, vol. 36. Washington, D.C.: Mineralogical Society of America. pp. 303–398.

Burchell M. J., Cole M. J., Price M. C., and Kearsley T. 2012. Experimental investigation of impacts by solar cell secondary ejecta on silica aerogel and aluminium foil: Implications for the Stardust Interstellar Dust Collector. *Meteoritics & Planetary Science* 47:671–683.

Butterworth A. L., Westphal A. J., Tyliszczak T., Gainsforth Z., Stodolna J., Frank D., Allen C., Anderson D., Ansari A., Bajt S., Bastien R. S., Bassim N., Bechtel H. A., Borg J., Brenker F. E., Bridges J., Brownlee D. E., Burchell M., Burghammer M., Changela H., Cloetens P., Davis A. M., Doll R., Floss C., Flynn G., Grün E., Heck P. R., Hillier J. K., Hoppe P., Hudson B., Huth J., Hvide B., Kearsley A., King A. J., Lai B., Leitner J., Lemelle L., Leroux H., Leonard A., Lettieri R., Marchant W., Nittler L. R., Ogliore R., Ong W. J., Postberg F., Price M. C., Sandford S. A., Sans Tresseras J., Schmitz S., Schoonjans T., Silversmit G., Simionovici A., Solé V. A., Srama R., Stephan T., Sterken V., Stroud R. M., Sutton S., Trieloff M., Tsou P., Tsuchiyama A., Vekemans B., Vincze L.,

Korff J. V., Wordsworth N., Zevin D., Zolensky M. E., and >30,000 Stardust@home dusters. 2014. Stardust Interstellar Preliminary Examination IV: Scanning Transmission X-ray Microscopy analyses of impact features in the Stardust Interstellar Dust Collector X-ray Microscopy. *Meteoritics & Planetary Science*, doi:10.1111/maps.12220.

Ebel D. S., Weisberg M. K., and Beckett J. R. 2012. Thermochemical stability of low-iron, manganese-enriched olivine in astrophysical environments. *Meteoritics & Planetary Science* 47:585–593.

Flynn G., Sutton S., Lai B., Brenker F. E., Burghammer M., Simionovici A., Schmitz S., Cloetens P., Lemelle L., Sans Tresseras J., Scho'onjans T., Silversmit G., Solé V. A., Vekemans B., Vincze L., Westphal A. J., Allen C., Anderson D., Ansari A., Bajt S., Bastien R. S., Bassim N., Bechtel H. A., Borg J., Bridges J., Brownlee D. E., Burchell M., Butterworth A. L., Changela H., Davis A. M., Doll R., Floss C., Frank D., Gainsforth Z., Grün E., Heck P. R., Hillier J. K., Hoppe P., Hudson B., Huth J., Hvide B., Kearsley A., King A. J., Leitner J., Leroux H., Leonard A., Lettieri R., Marchant W., Nittler L. R., Ogliore R., Ong W. J., Postberg F., Price M. C., Sandford S. A., Srama R., Stephan T., Sterken V., Stodolna J., Stroud R. M., Trieloff M., Tsou P., Tsuchiyama A., Tyliszczak T., Korff J. V., Wordsworth N., Zevin D., Zolensky M. E., and >30,000 Stardust@home dusters. 2014. Stardust Interstellar Preliminary Examination VII: Synchrotron X-ray Fluorescence Analysis of Six Stardust Interstellar Candidates Measured with the Advanced Photon Source 2-ID-D Microprobe. *Meteoritics & Planetary Science*, doi:10.1111/maps.12144.

Frank D., Westphal A. J., Zolensky M. E., Gainsforth Z., Bastien R. S., Allen C., Anderson D., Ansari A., Bajt S., Bassim N., Bechtel H. A., Borg J., Brenker F. E., Bridges J., Brownlee D. E., Burchell M., Burghammer M., Butterworth A. L., Changela H., Cloetens P., Davis A. M., Doll R., Floss C., Flynn G., Grün E., Heck P. R., Hillier J. K., Hoppe P., Hudson B., Huth J., Hvide B., Kearsley A., King A. J., Lai B., Leitner J., Lemelle L., Leroux H., Leonard A., Lettieri R., Marchant W., Nittler L. R., Ogliore R., Ong W. J., Postberg F., Price M. C., Sandford S. A., Tresseras J. S., Schmitz S., Schoonjans T., Silversmit G., Simionovici A., Solé V. A., Srama R., Stephan T., Sterken V., Stodolna J., Stroud R. M., Sutton S., Trieloff M., Tsou P., Tsuchiyama A., Tyliszczak T., Vekemans B., Vincze L., Korff J. V., Wordsworth N., Zevin D., and >30,000 Stardust@home dusters. 2013. Stardust Interstellar Preliminary Examination II: Curating the interstellar dust collector, picokeystones, and sources of impact tracks. *Meteoritics & Planetary Science*, doi:10.1111/maps.12147.

Gainsforth Z., Brenker F. E., Burghammer M., Simionovici A., Schmitz S., Cloetens P., Lemelle L., Sans Tresseras J., Schoonjans T., Silversmit G., Solé V. A., Vekemans B., Vincze L., Westphal A. J., Allen C., Anderson D., Ansari A., Bajt S., Bastien R. S., Bassim N., Bechtel H. A., Borg J., Bridges J., Brownlee D. E., Burchell M., Butterworth A. L., Changela H., Davis A. M., Doll R., Floss C., Flynn G., Frank D., Grün E., Heck P. R., Hillier J. K., Hoppe P., Hudson B., Huth J., Hvide B., Kearsley A., King A. J., Lai B., Leitner J., Leroux H., Leonard A., Lettieri R., Marchant W., Nittler L. R., Ogliore R., Ong W. J., Postberg F., Price M. C., Sandford S. A., Srama R., Stephan T., Sterken V., Stodolna J., Stroud R. M., Sutton S., Trieloff M., Tsou P., Tsuchiyama A., Tyliszczak T., Korff J. V., Wordsworth N., Zevin D., Zolensky M. E., and >30,000 Stardust@home dusters. 2014. Identification of crystalline material in two interstellar dust candidates from the Stardust mission. *Meteoritics & Planetary Science*, doi:10.1111/maps.12148.

Gruber D. E., Matteson J. L., Peterson L. E., and Jung G. V. 1999. The spectrum of diffuse cosmic hard X-rays measured with HEAO 1. *The Astrophysical Journal* 520:124–129.

Grün E., Zook H. A., Baguhl M., Balogh A., Bame S. J., Fechtig H., Forsyth R., Hanner M. S., Horanyi M., Kissel J., Lindblad B.-A., Linkert D., Linkert G., Mann I., McDonnell J. A. M., Morfill G. E., Phillips J. L., Polanskey C., Schwehm G., Siddique N., Staubach P., Svestka J., and Taylor A. 1993. Discovery of Jovian dust streams and interstellar grains by the ULYSSES spacecraft. *Nature* 362:428–430.

Ishii H. A., Bradley J. P., Dai Z. R., Chi M., Kearsley A. T., Burchell M. J., Browning N. D., and Molster F. 2008. Comparison of comet 81P/Wild 2 dust with interplanetary dust from comets. *Science* 319:447–450.

Joswiak D. J., Brownlee D. E., Matrajt G., Westphal A. J., Snead C. J., and Gainsforth Z. 2012. Comprehensive examination of large mineral and rock fragments in Stardust tracks: Mineralogy, analogous extraterrestrial materials, and source regions. *Meteoritics & Planetary Science* 47:471–524.

Klöck W., Thomas K. L., McKay D. S., and Palme H. 1989. Unusual olivine and pyroxene composition in interplanetary dust and unequilibrated ordinary chondrites. *Nature* 339:126–128.

Leroux H., Roskosz M., and Jacob D. 2009. Oxidation state of iron and extensive redistribution of sulfur in thermally modified Stardust particles. *Geochimica et Cosmochimica Acta* 73:767–777.

Lodders K. and Fegley B. 1998. *The planetary scientist's companion*. New York: Oxford University Press.

Markowicz A. and Van Grieken R. 2001. Quantification in XRF analysis of intermediate-thickness samples. In *Handbook of X-ray spectrometry*, 2nd ed., edited by Van Grieken R. and Markowicz A. New York: CRC Press. pp. 407–432.

Matsumoto M. and Nishimura T. 1998. Mersenne twister: A 623-dimensionally equidistributed uniform pseudorandom number generator. *ACM Transactions on Modeling and Computer Simulation* 8:3–30.

Schmitz S., Brenker F. E., Schoonjans T., Vekemans B., Silversmit G., Vincze L., Burghammer M., and Riekel C. 2009. In situ identification of a CAI candidate in 81P/Wild 2 cometary dust by confocal high resolution synchrotron X-ray fluorescence. *Geochimica et Cosmochimica Acta* 73:5483–5492.

Schoonjans T., Silversmit G., Vekemans B., Schmitz S., Burghammer M., Riekel C., Brenker F. E., and Vincze L. 2012. Fundamental parameter based quantification algorithm for confocal nano-X-ray fluorescence analysis. *Spectrochimica Acta Part B* 67:32–42.

Silversmit G., Vekemans B., Brenker F. E., Schmitz S., Burghammer M., Riekel C., and Vincze L. 2010. 3D elemental imaging of cometary matter by nanoscale X-ray fluorescence tomography. *ESRF Highlights* 15:114–115.

Simionovici A., Lemelle L., Cloetens P., Solé V. A., Sans Tresseras J., Butterworth A. L., Westphal A. J.,

Gainsforth Z., Stodolna J., Allen C., Anderson D., Ansari A., Bajt S., Bassim N., Bastien R. S., Bechtel H. A., Borg J., Brenker F. E., Bridges J., Brownlee D. E., Burchell M., Burghammer M., Changela H., Davis A. M., Doll R., Floss C., Flynn G., Frank D., Grün E., Heck P. R., Hillier J. K., Hoppe P., Hudson B., Huth J., Hvide B., Kearsley A., King A. J., Lai B., Leitner J., Leonard A., Leroux H., Lettieri R., Marchant W., Nittler L. R., Ogliore R., Ong W. J., Postberg F., Price M. C., Sandford S. A., Schmitz S., Schoonjans T., Schreiber K., Silversmit G., Srama R., Stephan T., Sterken V., Stroud R. M., Sutton S., Trieloff M., Tsou P., Tsuchiyama A., Tyliszczak T., Vekemans B., Vincze L., Korff J. V., Wordsworth N., Zevin D., Zolensky M. E., and >30,000 Stardust@home dusters. 2014. Stardust Interstellar Preliminary Examination VI: Quantitative elemental analysis by synchrotron X-ray fluorescence nanoimaging of eight impact features in aerogel. *Meteoritics & Planetary Science*, doi:10.1111/maps.12208.

Tsou P., Brownlee D. E., Sandford S. A., Horz F., and Zolensky M. E. 2003. Wild 2 and interstellar sample collection and Earth return. *Journal of Geophysical Research – Planets* 108:8113.

Vekemans B., Janssens K., Vincze L., Adams F., and Van Espen P. 1994. Analysis of X-ray spectra by iterative least squares (AXIL): New developments. *X-Ray Spectrometry* 23:275–285.

Westphal A. J., Snead C., Butterworth A., Graham G. A., Bradley J. P., Bajt S., Grant P. G., Bench G., Brennan S., and Pianetta P. 2004. Aerogel keystones: Extraction of complete hypervelocity impact events from aerogel collectors. *Meteoritics & Planetary Science* 39:1375–1386.

Westphal A. J., Allen C., Bastien R., Borg J., Brenker F., Bridges J., Brownlee D. E., Butterworth A. L., Floss C., Flynn G., Frank D., Gainsforth Z., Grün E., Hoppe P., Kearsley A., Leroux H., Nittler L. R., Sandford S. A., Simionovici A., Stadermann F., Stroud R. M., Tsou P., Tyliczszak T., Warren J., Zolensky M. E., and >23,000 Stardust@home dusters. 2008. Preliminary examination of the interstellar collection of Stardust (abstract #1391). 39th Lunar and Planetary Science Conference. CD-ROM.

Westphal A. J., Allbrink A., Allen C., Bajt S., Bastien R., Bechtel H., Bleuet P., Borg J., Bowker S., Brenker F., Bridges J., Brownlee D. E., Burchell M., Burghammer M., Butterworth A. L., Campanile A., Cloetens P., Cody G., Ferroir T., Ferrari K., Floss C., Flynn G. J., Frank D., Gainsforth Z., Gruumln E., Harmer M., Hoppe P., Kearsley A., Kulkarni S., Lai B., Lemelle L., Leroux H., Lettieri R., Marchant W., Mccreadie B., Nittler L. R., Ogliore R., Postberg F., Rigamonti C., Sandford S. A., Schmitz S., Silversmit G., Simionovici A., Sperry G., Srama R., Stadermann F., Stephan T., Stroud R. M., Susini J., Sutton S., Thompson V., Toucoulou R., Trieloff M., Tsou P., Tsuchiyama A., Tyliczszak T., Vekemans B., Vincze L., Warren J., Yahnke T., Zevin D., and Zolensky M. E. 2010. Non-destructive search for interstellar dust using synchrotron microprobes. *AIP Conference Proceedings* 1221:131–138.

Westphal A. J., Zolensky M. E., Gainsforth Z., Bastien R. S., Allen C., Anderson D., Ansari A., Bajt S., Bassim N., Bechtel H. A., Borg J., Brenker F. E., Bridges J., Brownlee D. E., Burchell M., Burghammer M., Butterworth A. L., Changela H., Cloetens P., Davis A. M., Doll R., Floss C., Flynn G., Frank D., Grün E., Heck P. R., Hillier J. K., Hoppe P., Hudson B., Huth J., Hvide B., Kearsley A., King A. J., Lai B., Leitner J., Lemelle L., Leroux H., Leonard A., Lettieri R., Marchant W., Nittler L. R., Ogliore R., Ong W. J., Postberg F., Price M. C., Sandford S. A., Tresseras J. S., Schmitz S., Schoonjans T., Silversmit G., Simionovici A., Solé V. A., Srama R., Stephan T., Sterken V., Stodolna J., Stroud R. M., Sutton S., Trieloff M., Tsou P., Tsuchiyama A., Tyliszczak T., Vekemans B., Vincze L., Korff J. V., Wordsworth N., Zevin D., and >30,000 Stardust@home dusters. 2014a. Final reports of the Stardust Interstellar Preliminary Examination. *Meteoritics & Planetary Science*, doi:10.1111/maps.12221.

Westphal A. J., Zolensky M. E., Gainsforth Z., Bastien R. S., Allen C., Anderson D., Ansari A., Bajt S., Bassim N., Bechtel H. A., Borg J., Brenker F. E., Bridges J., Brownlee D. E., Burchell M., Burghammer M., Butterworth A. L., Changela H., Cloetens P., Davis A. M., Doll R., Floss C., Flynn G., Frank D., Grün E., Heck P. R., Hillier J. K., Hoppe P., Hudson B., Huth J., Hvide B., Kearsley A., King A. J., Lai B., Leitner J., Lemelle L., Leroux H., Leonard A., Lettieri R., Marchant W., Nittler L. R., Ogliore R., Ong W. J., Postberg F., Price M. C., Sandford S. A., Tresseras J. S., Schmitz S., Schoonjans T., Silversmit G., Simionovici A., Solé V. A., Srama R., Stephan T., Sterken V., Stodolna J., Stroud R. M., Sutton S., Trieloff M., Tsou P., Tsuchiyama A., Tyliszczak T., Vekemans B., Vincze L., Korff J. V., Wordsworth N., Zevin D., and >30,000 Stardust@home dusters. 2014b. Stardust Interstellar Preliminary Examination I: Identification of tracks in aerogel. *Meteoritics & Planetary Science*, doi:10.1111/maps.12168.